Final Technical Report

USGS Award #G20AP00029

Updating the Geospatial Liquefaction Database and Model

Laurie G. Baise, Professor and Chair
Dept. Civil and Env. Engineering, Tufts University, 200 College Ave, Medford, MA, 02155
617-627-2211, 617-627-3994, laurie.baise@tufts.edu

Ashkan Akhlaghi and Alex Chansky, Graduate Student Researchers
Michele Meyer, Undergraduate Researcher
Babak Moeveni, Professor
Dept. Civil and Env. Engineering, Tufts University, 200 College Ave, Medford, MA, 02155

June 1, 2020 – December 31, 2021

Abstract

In recent years, the USGS and others (including the PI of this effort) have worked to develop predictive regional models for ground failure with a focus on landslides and liquefaction (Zhu et al., 2015, 2017; Nowicki et al., 2014). The models provide probability estimates of ground failure given the shaking from an earthquake event. The current USGS preferred models (Zhu et al., 2017 for liquefaction and Nowicki et al., 2014 for landslides) result in a probability estimate for the respective ground failure. The liquefaction probability is converted to a value that represents spatial extent as a percentage per pixel. The current USGS implementation includes the ground failure models as a product on the overview page for each earthquake on the USGS Earthquake Hazard Program website (as discussed by Wald et al., 2018; Allstadt et al. 2019). The USGS implementation provides evidence that a geospatial approach to liquefaction extent after an earthquake is a useful part of post-event earthquake response and communication. In the Zhu et al. (2017) geospatial liquefaction model (GGLM17), the models are based on a set of 27 earthquakes where the 2011 Tohoku earthquake and the 2011 Christchurch and Darfield earthquakes represent the most recent earthquakes with liquefaction occurrence in the liquefaction database. The GGLM17 also included earthquakes from 2014 and 2015 in California which did not experience liquefaction. In this work, we have updated the liquefaction database to include 51 earthquakes. The database includes 5 earthquakes which did not experience liquefaction. Using the enhanced database, we have provided an update to GGLM17 reflecting the new data. The updated model also uses logistic regression for model development. In addition to the explanatory variables evaluated in GGLM17, we also included elevation above water body, soil and sediment thickness (Pelletier et al. 2017), topographic roughness index, and topographic position index. In this work, the top performing best-fit model GGLM21a based on the AUC, Briar score, and AIC uses PGV, TRI, distance to closest water body, distance to river, and elevation above water body as the explanatory variables. The second best-fit model GGLM21b uses PGV, slope-based Vs30, distance to closest water body, distance to closest river, and elevation above closest water body as explanatory variables. These models (GGLM21a and GGLM21b) provide improved performance across both the 2017 and 2021 databases across the new inventory. We also evaluate regional bias. Performance is best for Japan, North America and Oceania. Performance is weaker (and the dataset is more limited) for Europe, South America.

Introduction

We have developed a regional liquefaction mapping approach that relies on broadly available geospatial parameters (Zhu et al., 2015; Zhu et al., 2017). Our work is based on the premise exemplified by previous work like Youd and Perkins (1978) that characterized the relationship between geologic depositional environments and liquefaction and Wald and Allen (2007) that demonstrated the relationship between soil properties and topography. As a direct precursor to our work, Knudsen and Bott (2011) found the likelihood of liquefaction is highly correlated with common geospatial features such as topographic slope and distance to the closest river. The geospatial liquefaction model relies on geospatial proxies for soil density and soil saturation combined with earthquake loading estimates from USGS ShakeMap to predict the spatial extent

of liquefaction after an earthquake. The soil saturation geospatial proxies are borrowed from the hydrology community and include the compound topographic index and a global estimate of water table depth. In addition, we evaluate geospatial proxies for saturation such as: elevation above closest water body, and distance to coast, distance to river, and distance to closest water body. The preferred soil density parameter is the slope-derived Vs30 derived by Wald and Allen (2007). Although geospatial proxies borrowed from the geomorphology including topographic position index (TPI) and topographic roughness index (TRI) are potentially useful. We also test global layers for soil and sediment thickness (Pelletier et al., 2016).

In our original work (Zhu et al. 2015), we developed a liquefaction occurrence/nonoccurrence database that was unbiased with respect to the spatial extent (i.e., complete coverage of liquefaction and nonliquefaction occurrence over the mapped area) using liquefaction from four earthquakes in Christchurch, New Zealand and Kobe, Japan. Using logistic regression and statistical goodness of fit metrics, we tested geospatial parameters as proxies for earthquake loading, soil density, and soil saturation and developed two predictive models: one for regional use and one for global use (herein referred to as GLM15). The model results provide a first-order estimate of the spatial coverage of liquefaction from simple geospatial parameters (peak ground acceleration, compound topographic index, and V_{s30}) and can be implemented for loss estimation and rapid response.

In the second rendition of the geospatial liquefaction model (Zhu et al., 2017, herein referred to as GLM17), the objective was to further improve the predictive performance of the geospatial liquefaction model, especially for generalization to new regions. In the Zhu et al. (2017) geospatial liquefaction model (GLM17), the model is based on a set of 27 earthquakes where the 2011 Tohoku earthquake and the 2011 Christchurch and Darfield earthquakes represent the most recent earthquakes with liquefaction occurrence in the liquefaction database. This expanded dataset was no longer spatially complete, so we needed to make some assumptions about sampling and the resulting model was developed using a balanced sample of liquefaction to nonliquefaction across the 27 events. GLM17 relied on PGV as the shaking parameter, slope-based Vs30 as the soil density parameter, and annual precipitation, distance to closest water body, and water table depth as the saturation parameters. GLM17 also uses thresholds where the probability of liquefaction is assigned the value of zero if PGV<3cm/s or Vs30>320 m/s.

The global geospatial liquefaction model developed by Zhu et al. 2017 (GGLM17) is described by the following equations:

$$P(x) = \begin{cases} \dfrac{1}{1+e^{-X}} & \text{If PGV} > 3 \text{ cm/s AND Vs30} < 620 \text{ m/s} \\ \\ 0 & \text{Otherwise} \end{cases}$$

(1)

P(x) is the probability of liquefaction which lies between zero and 1; and X includes explanatory variables that describes density, saturation and loading conditions and is given by:

$$X = 8.801 + a_1.ln(PGV) + a_2.ln(Vs30) + a_3.precipitation + a_4.distance\ to\ water + a_5.water\ table\ depth$$

(2)

Where the coefficients are listed in Table 1.

Table 1. Variables' coefficients used in the GGLM (Zhu et al., 2017)

Variable	Coefficient	unit
Ln (PGV)	0.334	cm/ s
Ln (Vs_{30})	-1.918	m/s
Precipitation	5.408^{-4}	mm
Distance to Water	-0.2054	km
Water table Depth	-0.0333	m

The liquefaction probability (P) is then converted to liquefaction spatial extent (LSE) using equation 3 as introduced by Zhu et al. (2017):

$$\text{LSE(P)} = \frac{49.15}{(1+42.4e^{-9.165(P)})^2}$$

(3)

Where P is the probability of liquefaction calculated by equation 1. This equation was derived by comparing probability values with observed liquefaction spatial extent from earthquakes with spatially complete maps (as discussed in Zhu et al., 2017). LSE after an earthquake is the spatial area covered by surface manifestations of liquefaction reported as a percentage of a pixel at a specific location on the map.

In Rashidian and Baise (2020), we compiled the initial dataset for this work and evaluated GLM17 performance across the expanded dataset. In that work, we found that the precipitation term tended to lead to high probabilities over wet regions and that liquefaction probabilities were high for small PGA values. As a result, two additional thresholds were added to the GLM17 model. When PGA is below 0.1g, liquefaction probability is assigned a value of zero. When annual precipitation is above 1700mm, overprediction is likely, so the annual precipitation should be capped at 1700mm.

In recent years, the USGS has adopted this work and that of others to develop predictive regional models for ground failure with a focus on landslides and liquefaction (Zhu et al., 2015, 2017; Nowicki et al., 2014). The current USGS implementation includes the ground failure models as a product on the overview page for each earthquake on the USGS Earthquake Hazard Program website (as discussed by Wald et al., 2018; Allstadt et al. 2019). The USGS implementation provides evidence that a geospatial approach to liquefaction extent after an earthquake is a useful part of post-event earthquake response and communication.

In this study, we present the expanded liquefaction inventory that includes 46 earthquakes. To develop the geospatial model, we sample the 46 liquefaction events for both liquefaction and nonliquefaction occurrence and supplement with five additional nonliquefaction events. Overall, this work includes 28 earthquakes that were not included in the Zhu et al. (2017) inventory. We

use a balanced sampling strategy where the more significant liquefaction events are undersampled so that they don't dominate the model. For each liquefaction occurrence and nonoccurrence, the geospatial proxies for earthquake loading, soil saturation, and soil density are sampled and the resulting dataset is used for model development. The geospatial model uses logistic regression where goodness of fit is evaluated with the Area Under the Curve (AUC) and the Briar Score.

Liquefaction Inventory
The liquefaction inventory builds on the past inventories developed by Zhu et al. (2015), Zhu et al. (2017), and Rashidian and Baise (2020). Table A1 in the appendix summarizes the earthquakes included in the liquefaction inventory. Spatial location of liquefaction occurrence was determined from primary sources which included digital files of points and polygons, or georeferenced points using latitude and longitude, or georeferenced points from scanned figures. Table A1 provides information on sources on georeferencing. Table A2 summarizes the earthquakes includes in our work as nonliquefaction events.

Sampling Liquefaction and Nonliquefaction Points

The liquefaction inventory includes both points and polygons. In order to sample the inventory to get liquefaction and nonliquefaction points, liquefaction points are used directly and liquefaction polygons are sampled on a 100 m grid. For sampling non-liquefaction points, a 1 km and 15 km buffer zone is applied to liquefaction points and polygons and the region between 1 km and 15 km is sampled on a grid with 1.5 km spacing. This is illustrated in Figure 1 and is consistent with the sampling in Zhu et al. (2017).

To manage the class imbalance across earthquakes with large liquefaction regions and large regions of nonliquefaction, liquefaction and non-liquefaction points of each event are downsampled to the maximum numbers of 2000 and 1000 points, respectively. Finally to make sure that each event has roughly equivalent influence on the modeling, liquefaction and non-liquefaction points are resampled so that the size of each event in the dataset is roughly the same. The resulting sampled database is summarized in Table 2.
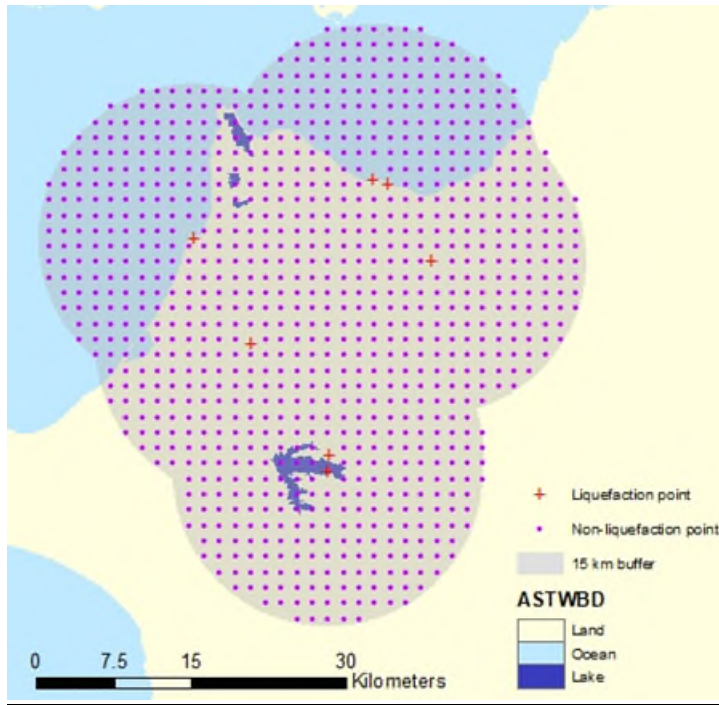
Figure 1. Example sampling of nonliquefaction points

Table 2. Liquefaction and nonliquefaction sampling

	Event Name	Date	M_w	Liquefaction Occurrence	Liquefaction Points	Sampled Liquefaction Points	Nonliquefaction Points	Sampled Nonliquefaction Points
1	Achaia	6/8/2008	6.5	Yes	7	7	662	662
2	Aquila	4/6/2009	6.3	Yes	4	4	321	321
3	Arequipa	6/23/2001	8.4	Yes	11	11	1489	1000
4	Baja	4/4/2010	7.2	Yes	50	50	1939	1000
5	Bhuj	1/26/2001	7.6	Yes	50358	2000	1938	1000
6	Central Italy	8/24/2016	6.2	No	0	0	2237	1000
7	Cephalonia	1/26/2014	6.1	Yes	12	12	210	210
8	Chichi	9/21/1999	7.6	Yes	1935	1935	2255	1000
9	Chiba	12/17/1987	6.5	Yes	624	624	1834	1834
10	Chino Hills	7/29/2008	5.4	No	0	0	2224	1000
11	Christchurch	2/22/2011	6.1	Yes	19278	2000	962	962
12	Darfield	9/3/2010	7	Yes	30506	2000	1554	1000
13	Denali	11/3/2002	7.9	Yes	40	40	4922	1000
14	Duzce	11/12/1999	7.2	Yes	3	3	636	636
15	Emilia	5/20/2012	6	Yes	58	58	809	809
16	Haiti	1/12/2010	7	Yes	13	13	735	735

17	Hector Mine	10/16/1999	7.1	No	0	0	2234	1000
18	Hokkaido	7/12/1993	7.7	Yes	1414	1414	3416	1000
19	Honduras	5/28/2009	7.3	Yes	13	13	539	539
20	Illapel	9/16/2015	8.3	Yes	5	5	646	646
21	Iquique	4/1/2014	8.2	Yes	11	11	867	867
22	Kobe	1/17/1995	6.9	Yes	6491	2000	2089	1000
23	Kocaeli	8/17/1999	7.6	Yes	36	36	1772	1000
24	Loma Prieta	10/17/1989	6.9	Yes	1088	1088	2842	1000
25	Maule	2/27/2010	8.8	Yes	72	72	13742	1000
26	Meinong	2/6/2016	6.3	Yes	12	12	585	585
27	Miyagi Ken	6/12/1978	7.6	Yes	104	104	1668	1000
28	Muisne	4/16/2016	7.8	Yes	13	13	1187	1000
29	Napa	8/24/2014	6	Yes	2	2	283	283
30	Nepal	4/25/2015	7.8	Yes	12	12	618	618
31	Niigata 1964	6/16/1964	7.6	Yes	10184	2000	3510	1000
32	Niigata 2004	10/23/2004	6.6	Yes	6110	2000	1533	1000
33	Niigata 2007	7/16/2007	6.6	Yes	281	281	737	737
34	Nihonkai	5/26/1983	7.7	Yes	9423	2000	2493	1000
35	Nisqually	2/28/2001	6.8	Yes	55	55	658	658
36	Northridge	1/17/1994	6.6	Yes	42	42	1761	1000
37	Oklahoma	9/3/2016	5.8	Yes	4	4	552	552
38	Piedmont	8/17/2015	4	No	0	0	1568	1568
39	Puget Sound 1949	4/13/1949	6.9	Yes	153	153	7982	1000
40	Puget Sound 1965	4/29/1965	6.7	Yes	228	228	6029	1000
41	Samara	9/5/2012	7.6	Yes	13	13	869	869
42	San Simeon	12/22/2003	6.6	Yes	20	20	226	226
43	Tecoman	1/22/2003	7.5	Yes	9	9	862	862
44	Telire Limon	4/22/1991	7.6	Yes	43	43	1447	1000
45	Tohoku	3/11/2011	9.1	Yes	46478	2000	5780	1000
46	Tokaichi	9/26/2003	8.3	Yes	147	147	4418	1000
47	Tottori	10/6/2000	6.7	Yes	916	916	979	979
48	Van Tab	10/23/2011	7.1	Yes	19	19	1158	1000
49	Virginia	8/23/2011	5.8	Yes	2	2	348	348
50	Wenchuan	5/12/2008	7.9	Yes	116	116	2135	1000
51	Yountville	9/3/2000	5	No	0	0	2135	1000

Geospatial Proxies

We use the same geospatial proxies that were used in Zhu et al. (2017) to estimate sediment density, sediment saturation, and earthquake loading with the addition of height above the nearest water table (zwb), and two proxies derived from a global sedimentary geology layer (Pelletier et al. 2016) that includes categorical variables such as uplands, lowlands and an estimate of sediment thickness. The geospatial proxies are summarized in Table 3 and illustrated for the San Francisco Bay area in Figure 2.

Table. 3. Potential Geospatial proxies

Variable Name	Variable Description	Density	Saturation	Load
Vs_{30}	Shear-wave velocity over the first 30 m	•		
Elev *(+std)*	Elevation	•		
slope	Topographic slope	•		
soil_thickness	Soil and sedimentary deposit thickness	•		
upland_lowland	Uplands vs. Lowlands	•		
TPI	Topographic Position Index	•		
TRI	Terrain Roughness Index	•		
dc	Distance to the nearest coast	•	•	
dr	Distance to the nearest river		•	
dwb	Distance to the nearest water body		•	
CTI	Compound topographic index		•	
wtd	Global water table depth		•	
zwb	Elevation above the nearest water body		•	
precip	Mean annual precipitation		•	
AI	Aridity index		•	
PGA *(+std)*	Peak ground acceleration			•
PGV *(+std)*	Peak ground velocity			•
Mw	Magnitude			•

Distance to the nearest coast is from a global data set created by the NASA's Ocean Color Group (2009). This data set was generated with the Generic Mapping Tools (GMT) software using its intermediate-resolution coastline. It was first computed at a spatial resolution of 0.04 degrees and then interpolated to 0.01 degrees. In the original dataset, negative distances represent locations over land (including land-locked bodies of water), while positive distances represent the ocean. For our application, we further process the data so that locations on land have positive distances and on ocean have zero distance.

Distance to the nearest river is calculated based on the HydroSHEDS database (Lehner et al. 2008). The development of this database includes a sequence of extensive hydrologic conditioning procedures to incorporate the locations of known rivers and lakes. The river network provided in this database is in vector format. Because distance computation using vector data at a global scale is inefficient, we derived a raster river network using the same threshold (100 upstream cells) and perform a raster distance calculation. Distance is in number of pixels and is a Cartesian distance.

Simulated water table depth is from a global dataset by Fan et al (2013). The authors simulate groundwater flow at 30 arc-seconds spacing using a model constrained by climate, terrain and sea level. Hydraulic conductivity of soil is estimated from a soil map and assuming a steady decay over depth. They digitized over 1.5 million published records of water table depths. The results have been adjusted using actual water-table depths as a means of calibration across climate zones

on all inhabited continents. This model predicts natural patterns of water table depth and so does not account for any pumping or irrigation carried out by humans. The data is at a spatial resolution of 30 arc-seconds. Mean annual precipitation is from a global layer developed by Hijmans et al. (2005). Hijmans et al. (2005) interpolated average monthly precipitation from weather stations across the world (47,554 locations) on a 30 arc-second resolution grid and averaged over the 1959-2000 time periods.

To model soil density, we derive the V_{S30} layer form a global DEM using the approach described by Wald and Allen (2007). The V_{S30} layer used in the development of GLM15 was based on GTOPO30. In GLM17, we update the V_{S30} layer by deriving it from the GMTED, a global DEM with enhanced quality. The GTOPO30 was initially developed in 1996 by the USGS, and the GMTED10 was recently developed by the USGS and NGA collaboratively to replace GTOPO30 as the elevation dataset for global application (Danielson and Gesch 2010). Therefore in this version, we use GMTED10 for the DEM.

The landform type (uplands/lowlands) and sedimentary thickness data are from a high-resolution gridded global data set developed by a multidisciplinary team at the University of Arizona (Pelletier et al., 2016). The data set is developed for regional and global land surface modeling and has a spatial resolution of 30 arcsec (~1 km). For the model development, Pelletier et al. (2016) explicitly mapped global landform types and then estimated the thicknesses of sedimentary deposit using models optimized for each landform type and the best available data for topography, climate, and geology as input. The sedimentary deposit thickness is within the range of 0-50 m, and areas with predicted sedimentary thickness greater than 50 m are assigned a value of 50 m. The dataset is archived at the Oak Ridge National Laboratory (ORNL) Distributed Active Archive Center (DAAC)
(https://daac.ornl.gov/SOILS/guides/Global_Soil_Regolith_Sediment.html).

To model earthquake shaking, we use PGA and PGV from ShakeMap, PGA is more frequently used in liquefaction modeling methods (e.g., Seed and Idriss, 1971) because it is proportional to the maximum shear stress induced in the sediment (Terzaghi et al., 1996). However, many studies show that PGV is a better predictor of liquefaction than PGA. Midorikawa and Wakamatsu, (1988) used PGA and PGV data from approximately 130 liquefaction sites and found PGV is better correlated with the occurrence of liquefaction. Bardet and Liu (2009) performed Monte Carlo simulation to study the relationship between the probability of liquefaction with other controlling parameters and found PGV is a more relevant indicator for characterizing the potential contribution of earthquakes. The reason might be liquefaction initiation is more sensitive to the low frequency components of the ground motion and the integration of the acceleration records to calculate velocity filters out higher frequencies. Bardet and Liu (2009) also observed nonlinear behavior between the PGV and empirical probability of liquefaction; As PGV increases, the probability of liquefaction first rapidly increases and then reaches a plateau when PGV is greater than a threshold (i.e., 10 cm/s). In our study, we add PGV as a candidate shaking proxy and compare the model with PGV and PGA as shaking proxies. We test different transformations of the shaking parameter and compare their performances.
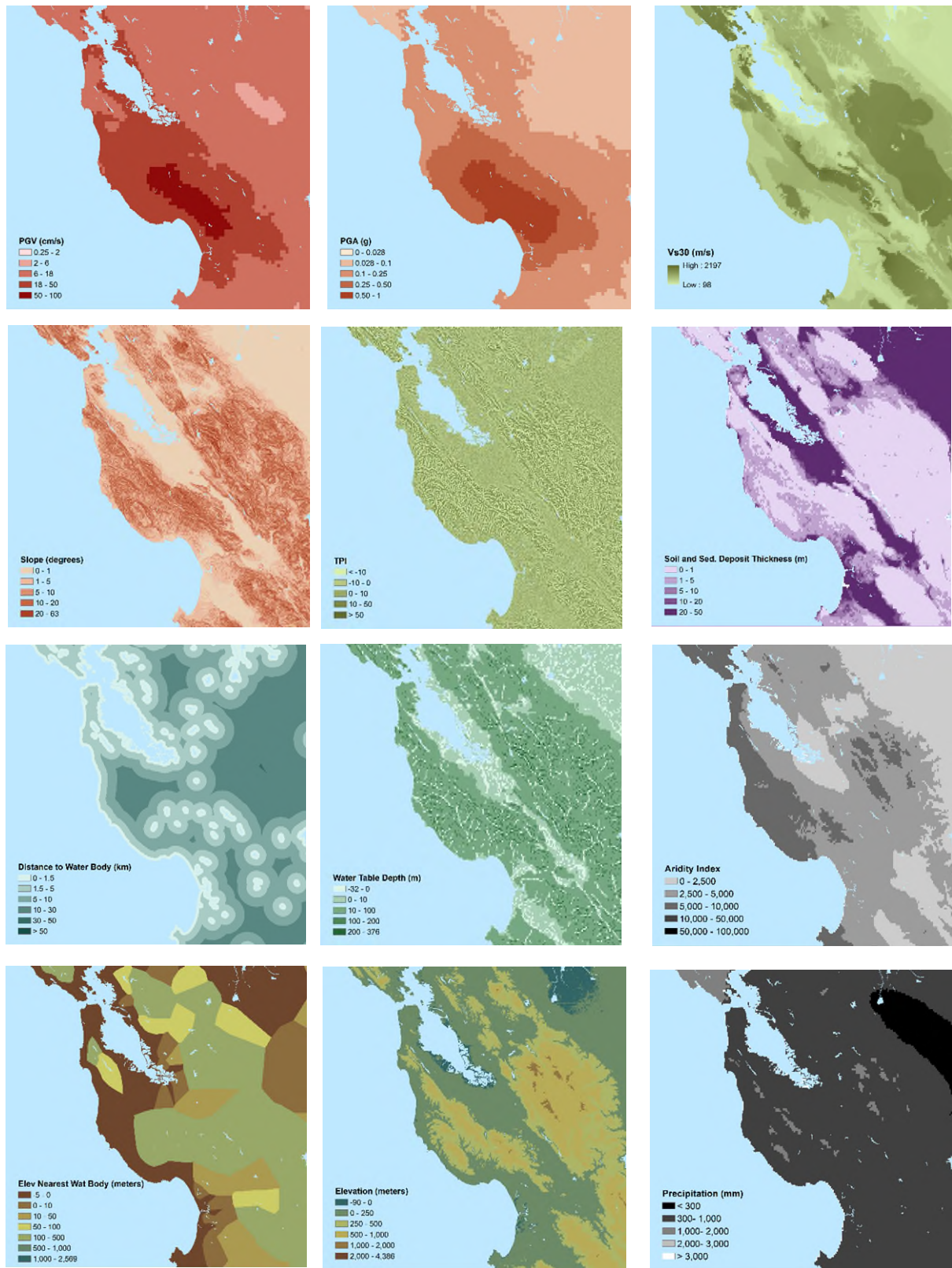
Figure 2. Geospatial proxies mapped for the greater San Francisco Bay

Exploratory Analysis

We explored the relationships between liquefaction and nonliquefaction across each of the potential geospatial proxies as a way of understanding which proxies were the most promising. This exploration is shown in Figure 3. Univariate logistic regression models are developed for each explanatory variable. Transformations are applied as shown in the x-axis. PGV, PGA, and Vs30 are lognormally transformed. TPI and TRI are transformed with the square-root of the absolute value. Dwb, Zwb, and elevation are transformed with the square-root transformation. Soil thickness, aridity, and precipitation are not transformed. The blue histogram represents nonliquefaction points. The orange histogram represents liquefaction points. The yellow dot represents the ratio of liquefaction to nonliquefaction points. And the purple line represents the best fit univariate logistic regression model for that geospatial proxy.

Based on the results of this exploratory analysis, ln(PGA) and ln(PGV) are the strongest proxy candidates for loading. TPI, TRI, Vs30 and slope are the strongest proxy candidates for soil density. Dwb (as well as dc and dr), Zwb, and wtd are the strongest candidates for soil saturation.
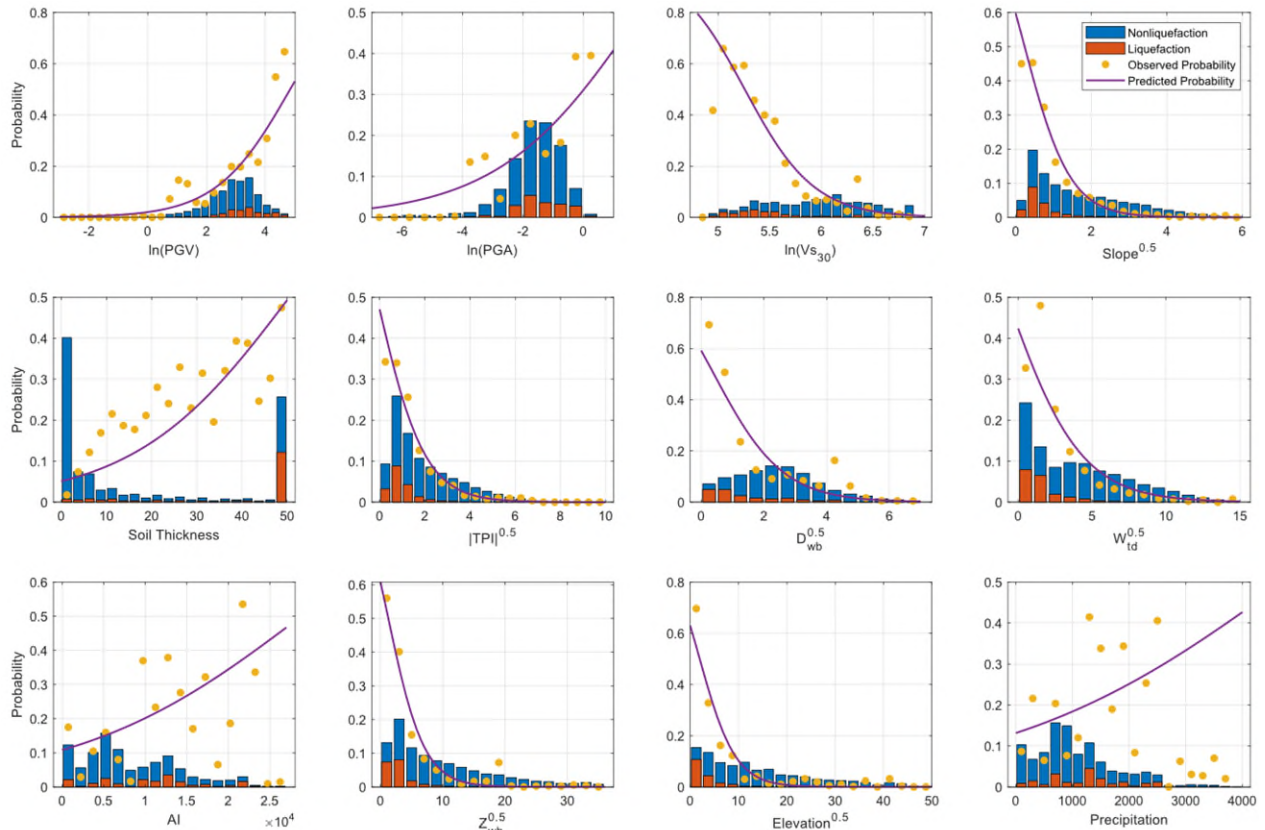

Figure 3. Exploratory analysis of each of the geospatial proxies. Univariate logistic regression models are developed for each explanatory variable. Transformations are applied as shown in the x-axis. The blue histogram represents nonliquefaction points. The orange histogram represents liquefaction points. The yellow dot represents the ratio of liquefaction to nonliquefaction points. And the purple line represents the best fit univariate logistic regression model for that geospatial proxy.

Performance Criteria

In this study, three different performance metrics have been used to guide us through the model building process: area under the ROC curve (AUC), Akaike information criterion (AIC), and the Brier score.

Receiver Operating Characteristics (ROC) curve which is one of the most commonly used performance measures in classification, plots the true positive rate (TPR) against the false positive rate (FPR) where:

$$TPR = \frac{True\ Positive}{True\ Positive + False\ Negative}$$

$$FPR = \frac{False\ Positive}{False\ Positive + True\ Negative}$$

Area under the ROC curve (AUC_{ROC}) can be used as a summary static to quantify the predictive capability of the model where AUC=1 represents the perfect classifier and AUC =0.5 relates to the completely uninformative classifier. ROC curves are helpful visual tools in understanding model's strength and weaknesses but using AUC_{ROC} as the only performance measure in model selection might not be ideal since models with close AUC values might have different predictive characteristics.

A common approach in performance assessment of statistical learning algorithms is to use metrics that penalize the learning algorithm based on its deviations from the correct predictions. AIC and Brier score use such an approach to quantify the model performance.

Akaike information criterion (AIC) (Akaike 1974) uses a logarithmic loss function for this purpose:

$$AIC = -2\boldsymbol{L} + 2k$$

Here k is the number of parameters in the model and $\boldsymbol{L}$ is the log likelihood for the probability predictions of the classification algorithm which for a binary classifier will be equal to:

$$\boldsymbol{L} = \sum y_i ln(\hat{y}_i) - (1 - y_i)ln\,(1 - \hat{y}_i)$$

Where y_i is the actual class identifier and $\hat{y}_i$ is the predicted probability of belonging to the class y=1.

Brier score (Brier 1950) uses a similar approach by calculating the mean squared error between the predicted probabilities and the actual class values:

$$Brier\ Score = \frac{1}{N} \sum (y_i - \hat{y}_i)^2$$

where N is the sample size. Since both AIC and Brier score are loss functions, lower values of them are related to better model performances (unlike AUC_{ROC}). While AIC values can go from 0 for the ideal classifier to infinity, Brier scores change between 0 (similarly for the ideal classifier) and 0.25 for the random classifier.

Candidate Models

Candidate models were generated using logistic regression to estimate the probabilities of liquefaction.

$$P(x) = \frac{1}{1+e^{-X}}$$

Here X is a linear combination of geospatial explanatory variables x_i. We evaluate different combinations of geospatial explanatory variables with a focus on determining optimal load variable combinations, density variable combinations, and saturation variable combinations using the strongest candidate geospatial proxies as found through the exploratory analysis.

In the current version of the models we do not retain the thresholds established in Zhu et al. (2017) around PGV and Vs30 as shown above. In the current liquefaction inventory, 1.5% of the liquefied data have PGV>3 cm/s and Vs30>620 m/s. Candidate models are presented in Table 4. Among the studied candidate models, there are tow models with similar performance: one including PGV, Vs_{30}, elevation from the closest water body (Z_{wb}) and distance from the river and distance to coast (D_r and D_c) and the other with Vs_{30} replaced with TRI.

Table 4. Goodness of fit for candidate models

Model Number	Load Variable	Density Variable	Saturation Variable	AUC	Brier	AIC
1	ln(PGA)	$TRI^{0.5}$	$Z_{wb}^{0.5}$	0.856	0.114	17,186
2	ln(PGA)	$TRI^{0.5}$	$ln(d_c+1)$, $ln(d_r+1)$	0.906	0.088	14,283
3	ln(PGA)	$TRI^{0.5}$	$ln(d_c+1)$, $ln(d_r+1)$, $Z_{wb}^{0.5}$	0.910	0.085	14,030
4	ln(PGA)	$ln(Vs_{30})$	W_{td}	0.857	0.110	17,329
5	ln(PGA)	$ln(Vs_{30})$	$ln(d_c+1)$, $ln(d_r+1)$	0.891	0.090	14,992
6	ln(PGA)	$ln(Vs_{30})$	$ln(d_c+1)$, $ln(d_r+1)$, W_{td}	0.901	0.088	14,563
7	ln(PGA)	$ln(Vs_{30})$	$ln(d_c+1)$, $ln(d_r+1)$, $Z_{wb}^{0.5}$	0.909	0.085	14,135
8	ln(PGV)	$TRI^{0.5}$	$Z_{wb}^{0.5}$	0.863	0.111	16,886
9	ln(PGV)	$TRI^{0.5}$	$ln(d_c+1)$, $ln(d_r+1)$	0.907	0.087	14,136
10	ln(PGV)	$TRI^{0.5}$	$ln(d_c+1)$, $ln(d_r+1)$, $Z_{wb}^{0.5}$	0.915	0.085	13,789
11	ln(PGV)	$ln(Vs_{30})$	W_{td}	0.859	0.109	17,156
12	ln(PGV)	$ln(Vs_{30})$	$ln(d_c+1)$, $ln(d_r+1)$	0.893	0.089	14,858
13	ln(PGV)	$ln(Vs_{30})$	$ln(d_c+1)$, $ln(d_r+1)$, W_{td}	0.902	0.088	14,463
14	ln(PGV)	$ln(Vs_{30})$	$ln(d_c+1)$, $ln(d_r+1)$, $Z_{wb}^{0.5}$	0.914	0.085	13,911

Based on these efforts, our recommended updated global geospatial liquefaction model (GGLM21) is described by the following equations:

$$P(x) = \frac{1}{1+e^{-X}}$$

$P(x)$ is the probability of liquefaction which lies between zero and 1; and X includes explanatory variables that describes density, saturation and loading conditions and is given by:

GGLM21a:

$$X_1 = \alpha_0 + \alpha_1. \ln(PGV) + \alpha_2.(TRI)^{0.5} + \alpha_3. \ln(d_c + 1) + \alpha_4. \ln(d_r + 1) + \alpha_5.(Z_{wb})^{0.5}$$

GGLM21b:

$$X_2 = \beta_0 + \beta_1. \ln(PGV) + \beta_2. \ln(Vs30) + \beta_3. \ln(d_c + 1) + \beta_4. \ln(d_r + 1) + \beta_5.(Z_{wb})^{0.5}$$

Where the coefficients are listed in Table 5. The standard error of the coefficients is calculated by taking 100 random samples from the inventory and then taking the mean and standard deviation of the resulting coefficients.

Table 5. Variable coefficients and standard error used in the GGLM21a and GGLM21b models

Model 1				Model 2			
Variable	Coefficient	SE	unit	Variable	Coefficient	SE	unit
intercept	4.925	8.14E-02	-	intercept	9.504	1.72E-01	-
ln (PGV)	0.694	1.37E-02	cm/ s	ln (PGV)	0.706	1.37E-02	cm/ s
TRI	-0.459	1.15E-02		ln (Vs30)	-0.994	3.05E-02	cm/s
d_c	-0.403	5.69E-03	m	d_c	-0.389	5.63E-03	m
d_r	-0.309	5.69E-03	m	d_r	-0.291	5.84E-03	m
Z_{wb}	-0.164	4.25E-03	m	Z_{wb}	-0.205	3.87E-03	m

Performance of the new model is also compared to the old model (Zhu et al. 2017) in Figure 4 and Table 6.
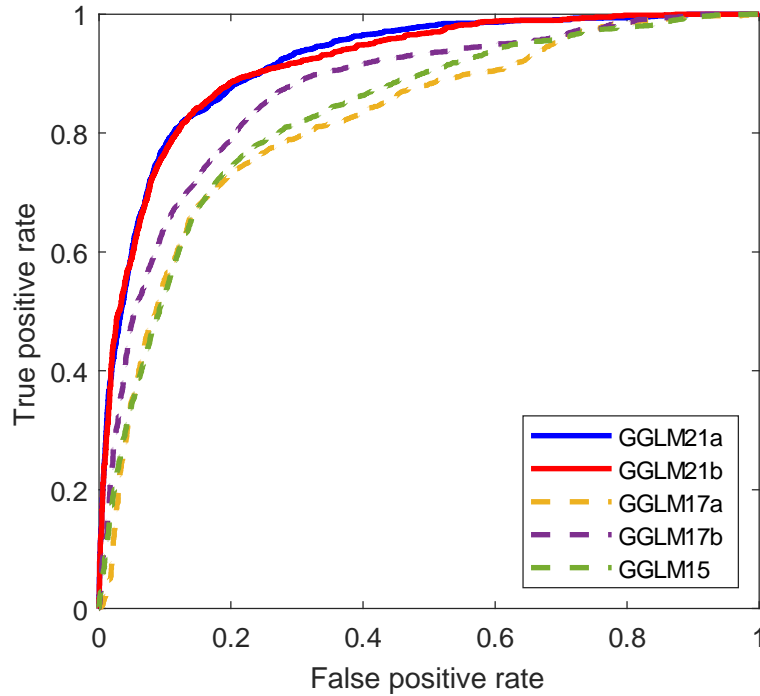
Figure 4. ROC Curve comparing GGLM15, GGLM17a and b (Zhu et al. 2017) and the updated models GGLM21a and GGLM21b. These are plotted using the updated GGLM21 database.

Table 6. Comparison of GGLM15, GGLM17a and GGLM17b with GGLM21a and GGLM21b across the new inventory

	AUC	Brier	AIC
GGLM 2021a	0.918	0.083	16,848
GGLM 2021b	0.915	0.084	17,278
GGLM 2017a	0.819	0.132	37,542
GGLM 2017b	0.868	0.105	21,828
GGLM 2015	0.832	0.124	28,556

Regional performance of the candidate models is shown in Figure 5 and summarized with accuracy statistics in Table 7. Both candidate models are compared with the proposed GGLM17b. Performance of the GGLM21 models is strongest in North America, Asia, Japan and Oceania. Performance in South America is stronger than the GGLM17b model but not as strong as other regions. Performance in Europe is comparable to GGLM17b. The inventory is smaller for South America and Europe.
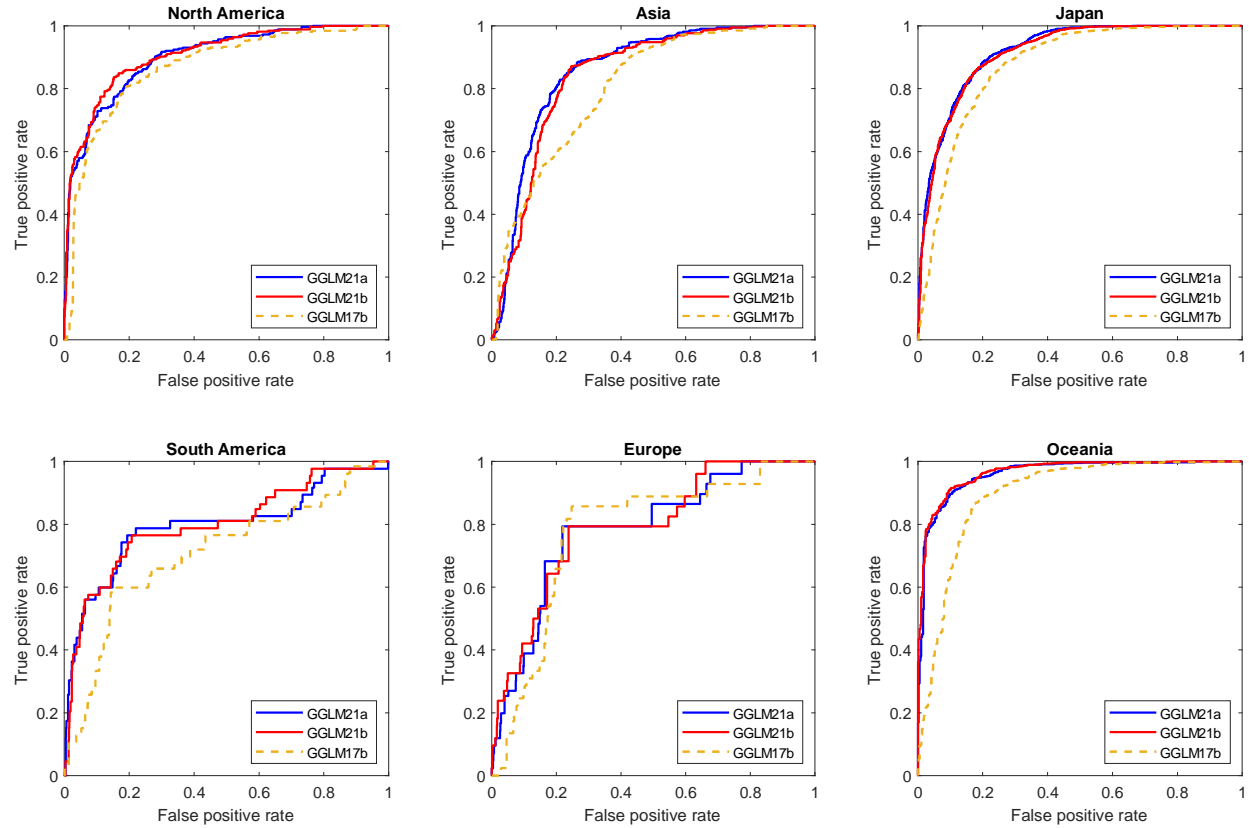
Figure 5. Regional performance of the candidate models

Table 7. Summary of regional performance of candidate models

	AUC			Brier			AIC		
	GGLM21a	GGLM21b	GGLM17b	GGLM21a	GGLM21b	GGLM17b	GGLM21a	GGLM21b	GGLM17b
Asia	0.859	0.844	0.805	0.144	0.151	0.172	2628	2707	3257
Europe	0.785	0.790	0.776	0.030	0.029	0.032	1260	1252	1266
Japan	0.919	0.914	0.874	0.123	0.124	0.176	4566	4669	6245
North America	0.900	0.907	0.868	0.055	0.052	0.055	3727	3582	3775
Oceania	0.961	0.966	0.896	0.209	0.218	0.419	1426	1480	2914
South America	0.796	0.800	0.709	0.047	0.049	0.044	1967	2132	1893

Conclusions

In this work, we have updated the liquefaction inventory to include 51 earthquakes. The database includes 5 earthquakes which did not experience liquefaction. In each of these earthquakes, we sample points that are classified as liquefied or not liquefied. Each location is also sampled for earthquake specific shaking parameters and geospatial parameters as proxies for soil density and soil saturation. In addition to the explanatory variables evaluated in GLM17, we also included elevation above water body, soil and sediment thickness (Pelletier et al. 2017), topographic roughness index, and topographic position index. Using the enhanced database, we have

provided an update to GLM17 reflecting the new data. We present two updated models which also use logistic regression for model development. In this work, the top performing best-fit model GGLM21a based on the AUC, Briar score, and AIC uses PGV, TRI, distance to coast, distance to river, and elevation above water body as the explanatory variables. The second best-fit model GGLM21b uses PGV, slope-based Vs30, distance to coast, distance to closest river, and elevation above closest water body as explanatory variables. These models provide improved performance across both the 2017 and 2021 databases.

Project Data
The liquefaction inventory will be supplied with the peer-reviewed journal publication as an electronic supplement. The journal publication is in preparation and will be submitted to the USGS when external review is complete.

Publications from project

Akhlaghi, M.M, Chansky, A., Baise, L., Moaveni, B., and Meyer, M. (2021). An updated to the Global Geospatial Liquefaction Model, SSA Annual Meeting.

References:
Akaike, H. (1974), "A new look at the statistical model identification", IEEE Transactions on Automatic Control, 19 (6): 716–723, doi:10.1109/TAC.1974.1100705.
Allstadt, K.E., E.M. Thompson, R.W. Jibson, D.J. Wald, M. Hearne, E.J. Hunter, J. Fee, H. Schovanec, Daniel Slosky, and Kirstie L. Haynie (2021; accepted). The USGS ground failure product: near-real-time estimates of earthquake-triggered landslides and liquefaction. *Earthquake Spectra*.
Bardet, J.P, F. Liu (2009) Motions of gently sloping ground during earthquakes. J. Geophys. Res. Earth Surf., 114 (2009), 10.1029/2008JF001107
Brier (1950). "Verification of Forecasts Expressed in Terms of Probability" (PDF). Monthly Weather Review. 78: 1–3. doi:10.1175/1520-0493(1950)078<0001:vofeit>2.0.co;2. Archived from the original (PDF) on 2017-10-23.
Fan, Y., H. Li, and G. Miguez-Macho (2013). Global patterns of groundwater table depth, Science 339, 940–943.
Hijmans, R. J., Cameron, S. E., Parra, J. L., Jones, P. G., and Jarvis, A., 2005, Very high resolution interpolated climate surfaces for global land areas: International Journal of Climatology, 25(15), 1965–1978.
Knudsen, K., and J. Bott (2011). Geologic and geomorphic evaluation of liquefaction case histories for rapid hazard mapping, Seismol. Res.Lett. 82, 334
Lehner, B., K. Verdin, and A. Jarvis (2006). HydroSHEDS Technical Documentation, World Wildlife Fund US, Washington, D.C.
Midorikawa, S. and Wakamatsu, K. 1988. Intensity of earthquake ground motion at liquefied sites, Soils and Foundations 28, 73–84.
Nowicki MA, Wald DJ, Hamburger MW, Hearne M, Thompson EM (2014) Development of a globally applicable model for near real-time prediction of seismically induced landslides. Eng Geol 173:54–65.
Pelletier, J. D., P. D. Broxton, P. Hazenberg, X. Zeng, P. A. Troch PA, G. Y. Niu, Z. Williams, M. A. Brunke, and D. Gochis (2016). A gridded global data set of soil, intact regolith, and sedimentary deposit thicknesses for regional and global land surface modeling, J. Adv. Model. Earth Syst. 8:41–65. https://doi.org/10.1002/2015MS000526
Rashidian, V. and Baise, L.G. (2020). Regional efficacy of a global geospatial liquefaction model. *Engineering Geology*. 272, 105644. https://doi.org/10.1016/j.enggeo.2020.105644..

Seed, H. B., and Idriss, I. M. (1971). ''Simplified procedure for evaluating soil liquefaction potential.'' J. Geotech. Engrg. Div., ASCE, 97(9), 1249–1273.

Terzaghi, K., Peck, R.B. and Mesri, G. (1996) Soil Mechanics in Engineering Practice. 3rd Edition, John Wiley and Sons, Inc., New York.

Wald, D.J., and Allen, T.I., 2007, Topographic Slope as a Proxy for Seismic Site Conditions and Amplification: Bulletin of the Seismological Society of America, 97 (5), 1379–1395.

Youd, T. L., and D. M. Perkins (1978). Mapping liquefaction-induced ground failure potential, J. Geotech. Eng. Div. 104, no. 4, Paper Number 13659, 433–446

Zhu, J., D. Daley, L. G. Baise, E. M. Thompson, D. J. Wald, and K. L. Knudsen (2015). A geospatial liquefaction model for rapid response and loss estimation, Earthq. Spectra 31, 1813–1837.

Zhu, J., Baise, L.G., Thompson, E.M., (2017). An Updated Geospatial Liquefaction Model for Global Application. Bull. Seismol. Soc. Am. 107 (3), 1365–1385

References for the liquefaction inventory are included in the tables in the Appendix.

Appendix

Table A1. Table of Earthquakes included in the database, including earthquake summary, and source information

#	Date	Mag.	Earthquake Name	Prior Inventory	Data source	Second reference	Shape
1	9/3/2010	7.0	Darfield	Zhu et al., 2015, 2017	Townsend, D., Lee, J.M., Strong, D.T., Jongens, R. et al (2016). Dataset S1	Zhu et al. 2015: the data for the 2010-2011 Darfield and Christchurch earthquakes from the Canterbury geotechnical database (https://canterburygeotechnicaldatabase.projectorbit.com; last accessed July 2014).	Polygons
2	2/22/2011	6.1	Christchurch	Zhu et al., 2015, 2017	Townsend, D., Lee, J.M., Strong, D.T., Jongens, R. et al (2016). Dataset S2	Zhu et al. 2015: the data for the 2010-2011 Darfield and Christchurch earthquakes from the Canterbury geotechnical database (https://canterburygeotechnicaldatabase.projectorbit.com; last accessed July 2014).	Polygons
3	1/17/1995	6.9	Kobe	Zhu et al., 2015, 2017	Hamada, M., Isoyama, R., and Wakamatsu, K., 1995. The 1995 Hyogo-ken Nanbu (Kobe) Earth-quake: Liquefaction, Ground Displacement and Soil Condition in the Hanshin Area, Assoc. for Development of Earthquake Prediction, Tokyo, 194 pp.		Points and Polygons
4	10/17/1989	6.9	Loma Prieta	Zhu et al., 2017	Tinsley et al. (1998). Maps and descriptions of liquefaction and associated effects. The Loma Prieta, California, Earthquake of October 17, 1989-Liquefaction. Edited by Thomas L. Holzer, USGS Professional Paper 1551-B		Polygons and points
5	4/13/1949	6.9	Puget Sound	Zhu et al., 2017	Chleborad, A. F., & Schuster, R. L. (1990). *Ground failure associated with the Puget Sound region earthquakes of April 13, 1949, and April 29, 1965* (No. 90-687). US Geological Survey.		Points

6	4/29/1965	6.7	Puget Sound	Zhu et al., 2017	Chleborad, A. F., & Schuster, R. L. (1990). *Ground failure associated with the Puget Sound region earthquakes of April 13, 1949, and April 29, 1965* (No. 90-687). US Geological Survey.		Points
7	2/28/2001	6.8	Nisqually	Zhu et al., 2017	Bray, J. D., Sancio, R., Kammerer, A. M., Merry, S., Rodriguez-Marek, A., Khazai, B., & Dreger, D. (2001). Some Observations of the Geotechnical Aspects of the February 28, 2001, Nisqually Earthquake in Olympia, South Seattle, and Tacoma, Washington. *Report sponsored by NSF, PEER Center, UCB, University of Arizona, Washington State University, Shannon and Wilson Inc., and Leighton and Associates.*		Points
8	1/17/1994	6.6	Northridge	Zhu et al., 2017	Stewart, J. P., Bray, J. D., Seed, R. B., & Sitar, N. (1994). Preliminary report on the principal geotechnical aspects of the January 17, 1994 Northridge earthquake. *University of California, Berkeley, Earthquake Engineering Research Center] Report UCB/EERC-94/08. Berkeley: Earthquake Engineering Research Center, University of California*	Stewart et al. (1996)	Polygons and points
9	12/22/2003	6.6	San Simeon	Zhu et al., 2017	Holzer, T. L., Noce, T. E., Bennett, M. J., Tinsley III, J. C., & Rosenberg, L. I. (2005). Liquefaction at Oceano, California, during the 2003 San Simeon earthquake. *Bulletin of the Seismological Society of America*, 95(6), 2396-2411		Polygons and points

10	7/12/1993	7.7	Hokkaido Nansei-oki	Zhu et al., 2017	Wakamatsu, K. (2011). Historic Liquefaction sites in Japan, 745-2008, University of Tokyo Press.	Polygons and points
11	12/17/1987	6.5	Chiba-ken-oki	Zhu et al., 2017	Wakamatsu, K. (2011). Historic Liquefaction sites in Japan, 745-2008, University of Tokyo Press.	Polygons and points
12	6/12/1978	7.6	Miyagi-ken-oki	Zhu et al., 2017	Wakamatsu, K. (2011). Historic Liquefaction sites in Japan, 745-2008, University of Tokyo Press.	Polygons and points
13	5/26/1983	7.7	Nihonkai Chubu	Zhu et al., 2017	Wakamatsu, K. (2011). Historic Liquefaction sites in Japan, 745-2008, University of Tokyo Press.	Polygons and points
14	10/23/2004	6.6	Niigata-ken Chuetsu 2004	Zhu et al., 2017	Wakamatsu, K. (2011). Historic Liquefaction sites in Japan, 745-2008, University of Tokyo Press.	Polygons and points

15	6/16/1964	7.6	Niigata 1964	Zhu et al., 2017	Wakamatsu, K. (2011). Historic Liquefaction sites in Japan, 745-2008, University of Tokyo Press.	Polygons and points
16	7/16/2007	6.6	Niigata 2007	Zhu et al., 2021	Wakamatsu, K. (2011). Historic Liquefaction sites in Japan, 745-2008, University of Tokyo Press.	Polygons and points
17	10/6/2000	6.7	Tottori-ken Seibu	Zhu et al., 2017	Wakamatsu, K. (2011). Historic Liquefaction sites in Japan, 745-2008, University of Tokyo Press.	Polygons and points
18	9/26/2003	8.3	Tokaichi-oki	Zhu et al., 2017	Wakamatsu, K. (2011). Historic Liquefaction sites in Japan, 745-2008, University of Tokyo Press.	Polygons and points
19	3/11/2011	9.1	Tohoku	Zhu et al., 2017	Ministry of Land, Transport and Tourism (MLITT) (2011)	Polygons and points

20	9/21/1999	7.6	Chi-Chi	Zhu et al., 2017	Chu, D. B., J. P. Stewart, S. Lee, J. S. Tsai, P. S. Lin, B. L. Chu, R. B. Seed, S. C. Hsu, M. S. Yu, and M. C. Wang (2004).Documentation of soil conditions at liquefaction and non-liquefaction sites from 1999 Chi–Chi (Taiwan) earthquake, Soil Dynam. Earthq. Eng. 24, 647–657.	Stewart P. J., Chu, D. B., Guglielmo, E., (2003). Documentation of soil conditions at liquefaction sites from 1999 Chi Chi (Taiwan) Earthquake, *Pacific Earthquake Engineering Research Center (digitized Figure 1)*	Polygons and points
21	1/26/2001	7.6	Bhuj	Zhu et al., 2017	Singh, R. P., S. Bhoi, and A. K. Sahoo (2002). Changes observed in land and ocean after Gujarat earthquake of 26 January 2001 using IRS data, Int. J. Rem. Sens. 23, 3123–3128 (digitized Figure 2b)		Polygons
22	8/24/2014	6	Napa	Zhu et al., 2017	Geo-Engineering Extreme Events Reconnaissance (GEER) Association (2014). Geotechnical Engineering Reconnaissance of the August 24, 2014 M 6 South Napa Earthquake, Rept No. GEER-037.		Points
23	5/12/2008	7.9	Wenchuan	Zhu et al., 2017	Cao, Z., L. Hou, H. Xu, and X. Yuan (2010). Distribution and characteristics of gravelly soil liquefaction in the Wenchuan Ms 8.0 earthquake, Earthq. Eng. Eng. Vib. 9, 167–175.	Chen LW, Yuan XM, Cao ZZ, et al. (2009), "Liquefaction Macrophenomena in the Great Wenchuan Earthquake," Earthquake Engineering and Engineering Vibration, (digitized Figure 1)	Points
24	11/3/2002	7.9	Denali (Alaska)	Rashidian and Baise (2020)	Kayen R, Thompson E, Minasian D, et al. Geotechnical Reconnaissance of the 2002 Denali Fault, Alaska, Earthquake. Earthquake Spectra. 2004;20(3):639-667.		Points
25	1/22/2003	7.5	Tecoman	Rashidian and Baise (2020)	Wartman J, Rodriguez-Marek A, Macari EJ, et al. Geotechnical Aspects of the January 2003 Tecomán, Mexico, Earthquake. Earthquake Spectra. 2005;21(2):493-538. (digitized Figure 4)		Points

26	4/4/2010	7.2	Baja California	Rashidian and Baise (2020)	Stewart, J. P., & Brandenberg, S. J. (2010). Preliminary report on seismological and geotechnical engineering aspects of the April 4 2010 mw 7.2 El Mayor-Cucapah (Mexico) earthquake. *Geotechnical Extreme Events Reconnaissance (GEER) Association* (digitized Figure)		Points
27	8/23/2011	5.8	Mineral, Virginia	Rashidian and Baise (2020)	Carter, M. and Maurer, B., 2011. Geotechnical Quick Report on the Affected Region of the 23 August 2011 M5. 8 Central Virginia Earthquake near Mineral, Virginia. Geotechnical Extreme Events Reconnaissance (GEER) Association. (Digitized Figure 1)		Points
28	9/3/2016	5.8	Oklahoma	Rashidian and Baise (2020)	Clayton, P., Zalachoris, G., Rathje, E., Bheemasetti, T., Caballero, S., Yu, X. and Bennett, S., 2016. The geotechnical aspects of the September 3, 2016 M 5.8 Pawnee, Oklahoma earthquake. GEER Association, Berkeley, California.		Points
29	6/23/2001	8.4	Arequipa	Rashidian and Baise (2020)	Gómez, J.C., Tavera, H.J., Orihuela, N., 2005. Soil liquefaction during the Arequipa Mw 8.4, June 23, 2001 earthquake, southern coastal Peru. Eng. Geol. 78 (3), 237–255. (digitized from Figure 1)		Points
30	2/27/2010	8.8	Maule	Rashidian and Baise (2020)	Verdugo, R., 2011. Comparing liquefaction phenomena observed during the 2010 Maule, Chile earthquake and 2011 Great East Japan earthquake. In: Proceedings of International Symposium on Engineering Lessons Learned from the (pp. 1-4).		Points

31	4/1/2014	8.2	Iquique	Rashidian and Baise (2020)	Rollins, K., Ledezma, C., Montalva, G., 2014. Geotechnical aspects of April 1, 2014, M8. 2 Iquique, Chile *Geotechnical Extreme Events Reconnaissance (GEER) Association.*	Franke, Kevin W., et al. "Reconnaissance of Two Liquefaction Sites Using Small Unmanned Aerial Vehicles and Structure from Motion Computer Vision Following the April 1, 2014 Chile Earthquake." Journal of Geotechnical and Geoenvironmental Engineering, American Society of Civil Engineers, 2 Dec. 2016, ascelibrary.org/doi/10.1061/%28ASCE%29GT.1943-5606.0001647.	Points
32	9/16/2015	8.3	Illapel	Rashidian and Baise (2020)	Candia, G., de Pascale, G., Montalva, G., Ledezma, C., 2015. Geotechnical Reconnaissance of the 2015 Illapel Earthquake. Geotechnical Extreme Events Reconnaissance (GEER) Association.		Points
33	4/16/2016	7.8	Muisne	Rashidian and Baise (2020)	Nikolaou, S., Vera-Grunauer, X., Gilsanz, R., Luque, R., Kishida, T., Diaz-Fanas, G., Alzamora, D., 2016. GEER-ATC M 7.8 April 16, 2016 Muisne, Ecuador Earthquake Reconnaissance Report. Geotechnical Extreme Events Reconnaissance (GEER) Association. GEER-049 doi:10.18118/G6F30N		Points
34	4/22/1991	7.6	Telire Limon	Rashidian and Baise (2020)	Yasuda, S., Watanabe, H., Yoshida, N., Mora, S., 1993. Soil Liquefaction During the 1991 Telire-Limón, Costa Rica, Earthquake. (Figure 2)		Points
35	5/28/2009	7.3	Honduras	Rashidian and Baise (2020)	Luna, R., 2010. Reconnaissance Report of the May 28, 2009 Honduras Earthquake, M 7.3. Geotechnical Extreme Events Reconnaissance (GEER) Association.		Points

36	1/12/2010	7.0	Haiti	Rashidian and Baise (2020)	Rathje, E., Bachhuber, J., Cox, B., French, J., Green, R., Olson, S., Rix, G., Wells, D., andSuncar, O., 2010. Geotechnical Reconnaissance of the 2010 Haiti Earthquake, GEER Association Report No. GEER-021.	Olson, S.M., Green, R.A., Lasley, S., Martin, N., Cox, B.R., Rathje, E., French, J., 2011. Documenting liquefaction and lateral spreading triggered by the 12 January 2010 Haiti earthquake. Earthquake Spectra 27 (S1), S93–S116.	Points
37	9/5/2012	7.6	Samara	Rashidian and Baise (2020)	Rollins, K., Franke, K., Luna, B.R., Rocco, N., Avila, D., Climent, M.R., 2013. Geotechnical Aspects of Sept. 5, 2012 m7.6 Samara, Costa Rica Earthquake. Geotechnical Extreme Events Reconnaissance (GEER) Association.	M 7.6 - Costa Rica (usgs.gov)	Points
38	8/17/1999	7.6	Kocaeli	Rashidian and Baise (2020)	Sonmez and Ulusay; 2008; Liquefaction potential at Izmit Bay: comparison of predicted and observed soil liquefaction during the Kocaeli earthquake.; Rathje, E.M., Karatas, I., Wright, S.G., Bachhuber, J., 2004. Coastal failures during the 1999 Kocaeli earthquake in Turkey. Soil Dyn. Earthq. Eng. 24 (9), 699–712.	C Scawthorn, G.S Johnson, Preliminary report: Kocaeli (Izmit) earthquake of 17 August 1999, Engineering Structures, Volume 22, Issue 7, 2000, Pages 727-745, ISSN 0141-0296, https://doi.org/10.1016/S0141-0296(99)00106-6 (http://www.sciencedirect.com/science/article/pii/S0141029699001066)	Points
39	11/12/1999	7.2	Duzce	Rashidian and Baise (2020)	Ghasemi et al.; The Nov 1999 Duzce Earthquake: Post-EQ investigation of the structures of the TEM https://www.fhwa.dot.gov/publications/research/infrastructure/structures/00146.pdf		Points
40	6/8/2008	6.5	Achia	Rashidian and Baise (2020)	Pavlides, S., Papathanassiou, G., Valkaniotis, S., Chatzipetros, A., Sboras, S., Caputo, R., 2013. Rock-falls and liquefaction related phenomena triggered by the June 8, 2008, M. Ann. Geophys. 56 (6), S0682.	Preliminary Report on the Principal Seismological and Engineering Aspects of the Mw=6.5 Achaia-Ilia (Greece) Earthquake on 8 June 2008	Points
41	4/6/2009	6.3	Aquila	Rashidian and Baise (2020)	Monaco, P., Santucci de Magistris, F., Grasso, S. et al. Analysis of the liquefaction phenomena in the village of Vittorito (L'Aquila). Bull Earthquake Eng 9, 231–261 (2011). https://doi.org/10.1007/s10518-010-9228-0	GEER Report Aquila	Points

42	10/23/2011	7.1	VanTab	Rashidian and Baise (2020)	Erdik, M., Kamer, Y., Demircioğlu, M. et al. 23 October 2011 Van (Turkey) earthquake. Nat Hazards 64, 651–665 (2012). https://doi.org/10.1007/s11069-012-0263-9	Aydan, Ö., Ulusay, R. & Kumsar, H. Seismic, ground motion and geotechnical characteristics of the 2011 Van-Erciş and Van-Edremit earthquakes of Turkey, and assessment of geotechnical damages. *Bull Eng Geol Environ* 73, 643–666 (2014). https://doi.org/10.1007/s10064-013-0526-z	Points
43	5/20/2012	6	Emilia	Rashidian and Baise (2020)	Papathanassiou, G., Caputo, R., Rapti-Caputo, D., 2012. Liquefaction phenomena along the paleo-Reno River caused by the May 20, 2012, Emilia (northern Italy) earthquake. Ann. Geophys. 55 (4).	Lai et al., 2012. Geotechnical aspects of May 20, 2020, M5.9 Emilia EQ, Italy. GEER Report.; Nat. Hazards Earth Syst. Sci., 13, 935–947, 2013 www.nat-hazards-earth-syst-sci.net/13/935/2013/ doi:10.5194/nhess-13-935-2013	Points
44	1/26/2014	6.1	Cephonia	Rashidian and Baise (2020)	George Papathanassiou, Athanassios Ganas, Sotirios Valkaniotis, Recurrent liquefaction-induced failures triggered by 2014 Cephalonia, Greece earthquakes: Spatial distribution and quantitative analysis of liquefaction potential, Engineering Geology, Volume 200, 2016, Pages 18-30, ISSN 0013-7952, https://doi.org/10.1016/j.enggeo.2015.11.011.	GEER/ERI/ATC EARTHQUAKE RECONNAISSANCE REPORT,L 2012, ITALY	Points
45	4/25/2015	7.8	Nepal	Rashidian and Baise (2020)	Hashash et al., 2015; Geotechnical Field Reconnaissance: Gorkha (Nepal) Earthquake of April 25 2015 and Related Shaking Sequence. GEER.		Points
46	2/6/2016	6.3	Meinong	Rashidian and Baise (2020)	Sun, J., Hutchinson, T., Clahan, K., Menq, F., Lo, E., Chang, W.J., Ma, K.F., 2016. Geotechnical Reconnaissance of the 2016 Mw6. 3 Meinong Earthquake, Taiwan. Geotechnical Extreme Events Reconnaissance (GEER) Association.	Chi-Chin Tsai, Shang-Yi Hsu, Kuo-Lung Wang, Hsuan-Chih Yang, Wei- Kuang Chang, Chia-Han Chen & Yu-Wei Hwang (2017): Geotechnical Reconnaissance of the 2016 ML6.6 Meinong Earthquake in Taiwan, Journal of Earthquake Engineering, DOI: 10.1080/13632469.2017.1297271	Points

Table A2. Nonliquefaction events used in this study

Date	Magnitude	Earthquake Name	Source
9/3/2000	5	Yountville	
8/17/2015	4	Piedmont	
7/29/2008	5.4	Chino Hills	Geo-Engineering Extreme Events Reconnaissance (GEER) Association (2008). Preliminary Geotechnical Observations of the July 29, 2008 Southern California Earthquake, available at http://www .geerassociation.org/images/GEER_Activities/07-29-2008%20LA% 20EQ/ChinoHillsEarthquakeFinal.pdf (last accessed March 2017).
10/16/1999	7.1	Hector Mine	
8/24/2016	6.2	Central Italy	Zimmaro, P., & Stewart, J. P. (2016). Engineering reconnaissance following the 2016 M 6.0 Central Italy Earthquake. *Geotechnical Extreme Events Reconnaissance (GEER) Association*